International Journal of Fatigue 175 (2023) 107821

Contents lists available at ScienceDirect

International Journal of Fatigue

journal homepage: www.elsevier.com/locate/ijfatigue

Nanograin formation mechanism under fatigue loadings in additively manufactured Ti-6Al-4V alloy

Weiqian Chi [a], Wenjing Wang [a,*], Lei Wu [b], Guihua Duan [c], Chengqi Sun [c,d,*]

[a] Key Laboratory of Vehicle Advanced Manufacturing, Measuring and Control Technology (Beijing Jiaotong University), Ministry of Education, Beijing 100044, China
[b] Guobiao (Beijing) Testing & Certification Co., Ltd., Beijing 101400, China
[c] State Key Laboratory of Nonlinear Mechanics, Institute of Mechanics, Chinese Academy of Sciences, Beijing 100190, China
[d] School of Engineering Science, University of Chinese Academy of Sciences, Beijing 100049, China

ARTICLE INFO

Keywords:
Additively manufactured titanium alloy
Very high cycle fatigue
Crack initiation
Twinning
Nanograin formation

ABSTRACT

Quasi in-situ observation indicates that the basal slips, prismatic slips and pyramidal ⟨**a**⟩ slips are main slip types in α grains, and twinning tends to occur in α grains with *c*-axis nearly parallel to the applied stress for additively manufactured Ti-6Al-4V alloy in low cycle fatigue regime. The slip induces dense dislocation of cells or walls, and the deformation twinning leads to subgrains with higher misorientation. Nanograins with low-angle grain boundaries (2°–10°) and {10$\bar{1}$2} twins are also found in very high cycle regime. The slip and deformation twinning are both contributors to the nanograin formation during fatigue loadings.

1. Introduction

Additively manufactured (AM) titanium alloys present a large potential use in aerospace and biomedical industries, due to the shorter production cycle of AM technique in small lot sizes or parts with complicated geometries and the excellent mechanical properties of titanium alloys [1]. However, some of the components bear high cycle fatigue (HCF) and very high cycle fatigue (VHCF) loadings in these fields [2,3], and the fatigue performance determines the application of titanium alloys to an extent [4]. Hence, the elucidation of the fatigue crack initiation mechanism is vital for improving the fatigue resistance of AM titanium alloys.

Currently, the AM titanium alloys could be comparable to the conventionally processed Ti alloy by eliminating or reducing the manufacturing defects effectively through the process of hot-isostatic pressing (HIP) [5–8]. It has been shown that the fatigue crack usually does not initiate from the AM defects for HIP AM alloys, and the fracture surface often exhibits the fine granular area (FGA) feature for the crack initiation and early growth region in VHCF regime [3,5,9]. FGA consumes almost all the fatigue life in VHCF regime [9,10]. While the slip or cleavage of α grains induced crack initiation mechanism in low cycle fatigue [11,12] and in HCF [13] cannot give a reasonable explanation for the observation of nanograins with various orientations formed in the crack initiation and early growth region of titanium alloys [5,10,14–18]. The recent results indicated that the deformation twins played a vital role in the process of grain refinement during crack initiation and early growth at VHCF of Ti alloys [18]. The role of twinning during crack initiation was also investigated in medium-entropy alloys [19] and Mg alloys [20]. However, there are no results of the direct in-situ observation for the process of twinning formation and grain refinement during fatigue loadings.

Motivated by the above considerations, the quasi in-situ electron backscatter diffraction (EBSD) was used to investigate the twinning and slipping process at pre-selected specific locations during fatigue loadings and therefore to explore the fatigue induced nanograin formation mechanism in AM titanium alloys. Moreover, the microstructure near the fracture surface at the crack initiation region was observed for VHCF specimens under a positive stress ratio by a combined use of scanning electron microscope (SEM), focused ion beam (FIB), and transmission Kikuchi diffraction (TKD) method. Further transmission electron microscope (TEM) and high resolution transmission electron microscope (HRTEM) observation shows that the twin boundary (TB) presents serrated character. The studies provide an understanding of the processing of grain refinement on the HCF and VHCF crack initiation

* Corresponding authors at: Key Laboratory of Vehicle Advanced Manufacturing, Measuring and Control Technology (Beijing Jiaotong University), Ministry of Education, Beijing, 100044, China (W. Wang); State Key Laboratory of Nonlinear Mechanics, Institute of Mechanics, Chinese Academy of Sciences, Beijing 100190, China (C. Sun).
E-mail addresses: wjwang@bjtu.edu.cn (W. Wang), scq@lnm.imech.ac.cn (C. Sun).

https://doi.org/10.1016/j.ijfatigue.2023.107821
Received 31 March 2023; Received in revised form 30 June 2023; Accepted 2 July 2023
Available online 3 July 2023
0142-1123/© 2023 Elsevier Ltd. All rights reserved.

mechanism in AM titanium alloys.

2. Materials and methods

2.1. Materials

The material used in this study is an AM Ti-6Al-4V alloy made by selective laser melting technology on a BLT-S310 machine [10,21]. Processed parts were cylindrical with 12 mm in diameter and 100 mm in height. Then, they were heat-treated for 2 h at 710 °C in vacuum, and finally treated by HIP at 920 °C and 1000 bar for 2 h in argon atmosphere. The tensile strength and yield strength are obtained from three tensile specimens, and the values are 946 ± 5.86 MPa and 846 ± 14.53 MPa, respectively. The error bars were calculated using standard deviation. Fig. 1a shows the inverse pole figure (IPF) of the basketweave microstructure with thin α-grain laths of the present AM Ti-6Al-4V alloy along the loading direction (direction of reference coordinate system X in Fig. 1a), and the corresponding band contrast map, phase map and kernel average misorientation (KAM) map are shown in Fig. 1b–d, respectively. It indicates that the proportion of β phase is very small, and the plastic deformation is not significant for the original material.

2.2. Testing methods and characterization

All the fatigue tests were conducted in air and at room temperature and the stress ratio is 0.1. The ultrasonic specimens and the quasi in-situ specimen were used to explore the nanograin formation mechanism of the AM Ti-6Al-4V alloy, as shown in Fig. 2a and b, respectively. The

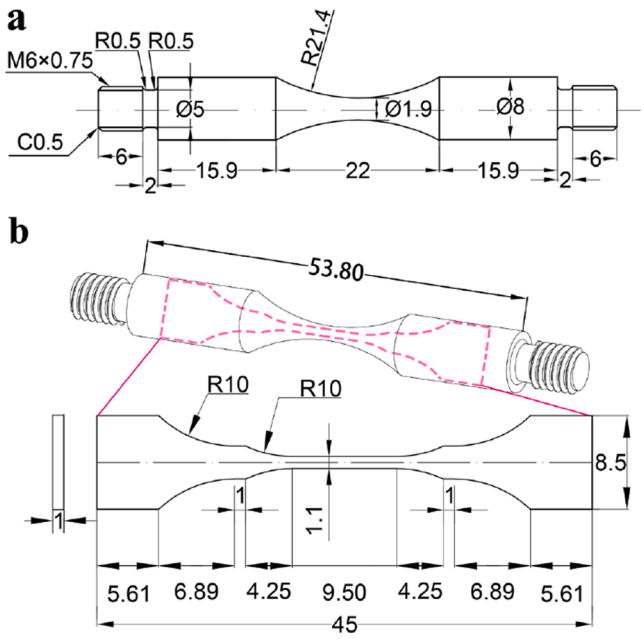

Fig. 2. Sketch maps of fatigue specimens (in mm). (a) Specimens for ultrasonic frequency fatigue test. (b) Specimens for quasi in-situ fatigue test.

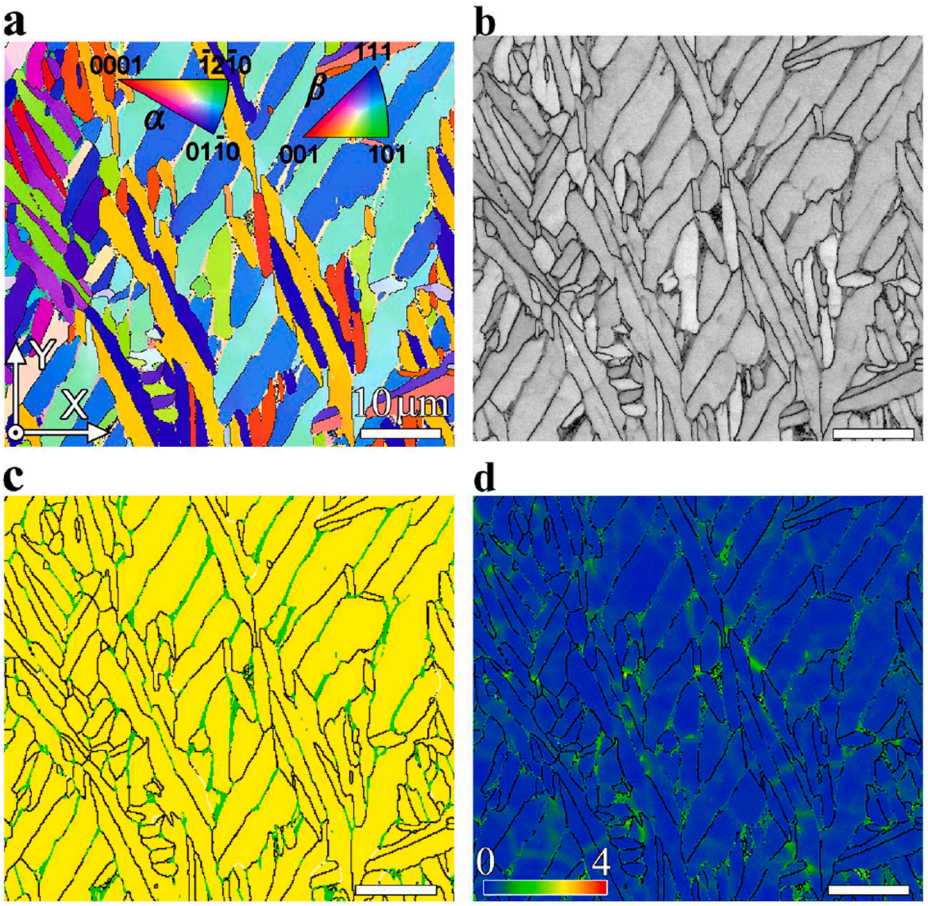

Fig. 1. EBSD results of microstructure without experiencing fatigue loadings. (a) Inverse pole figure (IPF). (b) Band contrast map. (c) Phase map (α phase: yellow, β phase: green). (d) KAM map of the microstructure. (For interpretation of the references to color in this figure legend, the reader is referred to the web version of this article.)

ultrasonic specimens were performed by an ultrasonic frequency fatigue test system USF-2000A ($f = 20$ kHz), and an adjustable cooling system was used to reduce the temperature of the specimen during the fatigue tests. The quasi in-situ specimen was performed by SERVO-SEM ($f = 10$ Hz), and then the labeled regions were observed by SEM and EBSD after a certain loading cycles. It is worth noting that the quasi in-situ specimen was extracted from an ultrasonic sample (Fig. 2b) and the microstructure after VHCF loadings is also examined.

After ultrasonic fatigue tests, the fracture surfaces of specimens were observed by SEM, FIB (Helios Nanolab 600i), and TKD techniques to obtain the cross-section microstructure of the crack initiation site to reveal the VHCF crack initiation mechanism. The quasi in-situ EBSD specimen was first ground by the abrasive papers with a water lubricant and then polished by 0.25 μm OP-S suspension and by the VibroMet 2 vibratory for about 6 h. Three FIB samples were extracted from the region where twinning, slipping, and subgrain formation occurred in the quasi in-situ region for a further TEM, HRTEM and TKD analysis.

EBSD was performed using ZEISS Gemini SEM 300 fitted with Oxford Instruments Symmetry S1 detector. The accelerating voltage was 20 kV, the scan step size was 150 nm, and the magnification was 1500× for the microstructure observation of the original material. The acceleration voltage was 20 kV, the step size was 300 nm at 500×, and the step size was 80 nm at 1500× for the quasi in-situ observation. For TKD observation, the accelerating voltage was 30 kV and the scan step size was 15 nm. The magnification was 7.82 k× for the extracted sample in the crack initiation and early growth region in VHCF regime and 8.50 k× for the extracted samples from the quasi in-situ region, respectively. The EBSD and TKD data were analyzed using HKL CHANNEL5 software. TEM and HRTEM observations were performed using the JEM-2100F microscope at 200 kV.

3. Experimental results and analyses

3.1. S-N data of ultrasonic specimens and the quasi in-situ specimen

The stress-life data are shown in Fig. 3 and the detailed information on the stress amplitude and fatigue life are shown in Table 1. The stress amplitude is taken as that of the gauge section. The S-N date of ultrasonic specimens presents a high linear correlation at higher stress amplitude in the log–log scale and shows a plateau region feature after 10^9 cycle loading. For a direct capture of the process of nanograin formation during fatigue loadings, the quasi in-situ specimen (Fig. 2b) was extracted from the unbroken ultrasonic specimen (Fig. 2a) which has experienced 1.01×10^9 loading cycles at $\sigma_{max} = 750$ MPa under the ultrasonic frequency fatigue test as shown in Fig. 3.

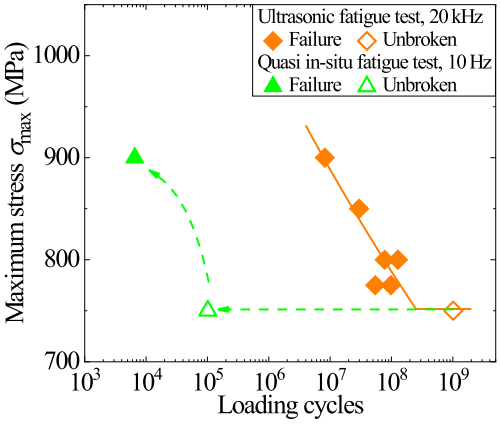

Fig. 3. Stress-life data, in which the median S-N curve is fitted by the bilinear relation of the S-N data in log–log scale [22], and the green dash line denotes the further in-situ test for the unbroken specimen after ultrasonic frequency fatigue test. (For interpretation of the references to color in this figure legend, the reader is referred to the web version of this article.)

Table 1
Stress amplitude σ_a, and fatigue life N_f for ultrasonic specimens and the in-situ specimen.

Ultrasonic frequency fatigue test			Quasi in-situ fatigue test		
Specimen No.	σ_a (MPa)	N_f	Specimen No.	σ_a (MPa)	N_f
1	900	8.20×10^6	1*	750	1.01×10^5
2	850	2.97×10^7	1**	900	6.56×10^4
3	800	7.75×10^7			
4	775	5.43×10^7			
5	775	9.80×10^7			
6	800	1.27×10^8			
7*	750	1.01×10^9			

* It denotes that the specimen does not fail at the tested fatigue cycles. ** It denotes that the specimen is then tested at a higher stress amplitude.

3.2. Nanograin formation in VHCF regime

SEM observation shows that the failed specimens all present internal crack initiation with FGA morphologies in HCF and VHCF regimes, similar to the results of the HIP AM Ti-6Al-4V alloy at $R = -1$ and the non-HIP AM Ti-6Al-4V alloy at $R = 0.1$ [5,10]. This indicates that the non-defect induced cracking also presents the FGA feature in the crack initiation and early growth region at a positive stress ratio in AM titanium alloys. For a further understanding of the microstructure in FGA, a micro-sample is extracted in FGA along the loading direction as shown in Fig. 4a–d by FIB technique. As commonly observed for the VHCF of AM titanium alloys [5], the nanograins are found in the crack initiation and early growth region near the fracture surface, as shown in the TKD results in Fig. 4e–g. The micro-crack formation is also observed within the nanograins beneath the fracture surface (Fig. 4c–g). These results indicate that the nanograins play an important role in the VHCF crack initiation and early growth of AM titanium alloys. The fatigue crack could initiate within the nanograin regions and the boundaries between the nanograin and the coarse grain regions due to the increase of the microstructure inhomogeneity and stress concentration caused by the formation of nanograins [10,18,23,24]. Further analysis of the EBSD results indicates that deformation twinning appears in the α grains at the fracture surface in FGA.

The twinning mode is identified via the HKL CHANNEL5 software. The twinning type in hexagonal close-packed (HCP) structure can be described by an 85° rotation about $\langle \bar{1}2\bar{1}0 \rangle$, which indicates the $\{10\bar{1}2\}\langle \bar{1}011 \rangle$ extension twinning. Moreover, the KAM map in Fig. 4h indicates a larger dislocation density around the twins and nanograins. This could be due to that the twinning and grain refinement increase the numbers of grain boundaries, and these boundaries restrain the dislocation slip [23,25].

3.3. Quasi in-situ observation of nanograin formation

It has been shown that the nanograins can be formed due to twinning for α phase in titanium alloys during VHCF regime [18,26]. Here, the quasi in-situ EBSD observation fatigue tests were conducted to capture the microstructure and damage evolution during fatigue loadings. Several marks were at first made on the quasi in-situ specimen surface using the microhardness indents (Fig. 5a) for quickly locating the same region during fatigue loadings. Fig. 5d–g shows the SEM image, IPF and KAM map of the labelled region in the quasi in-situ specimen extracted

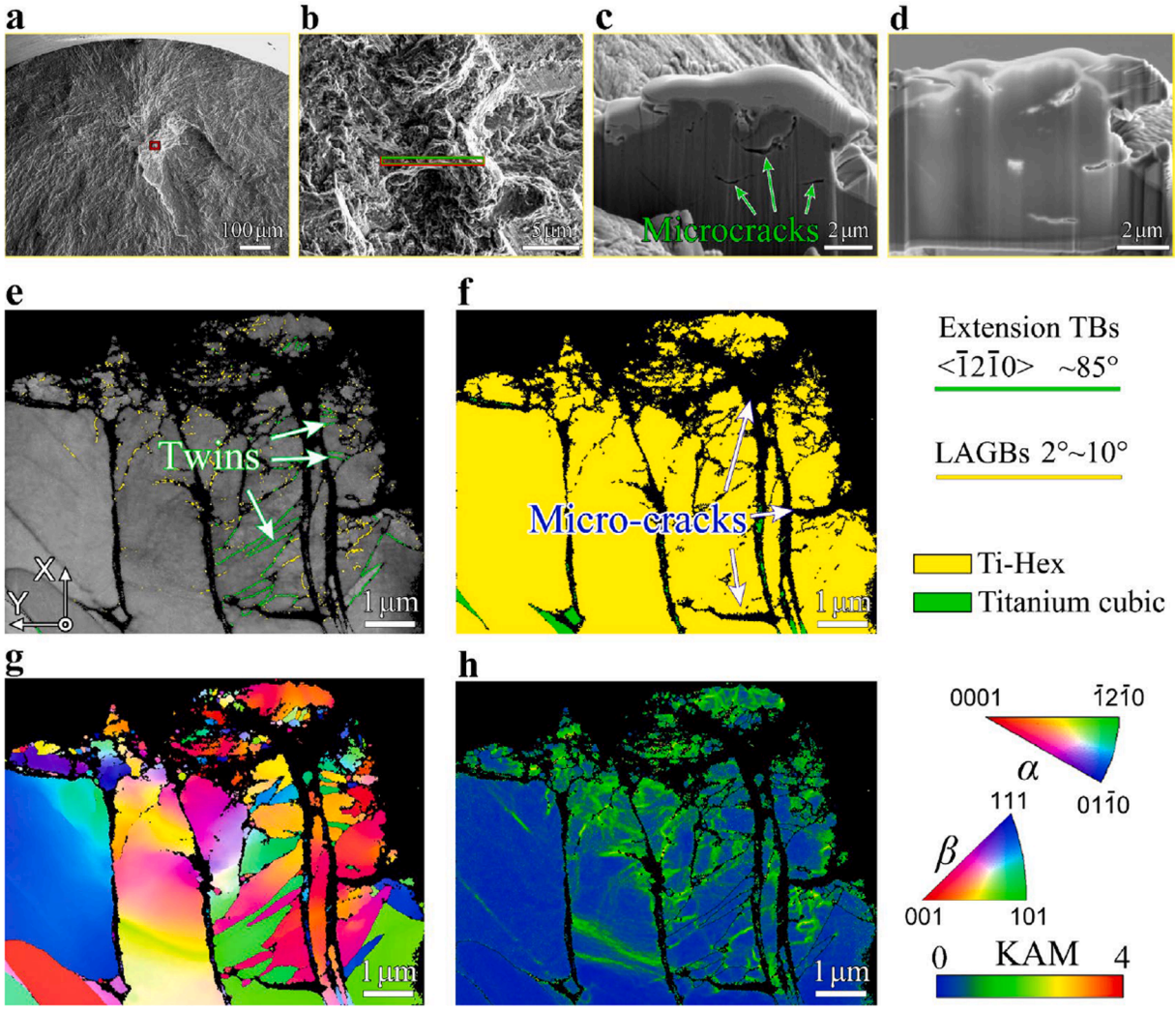

Fig. 4. SEM and EBSD observation of the specimen failed at $\sigma_{max} = 800$ MPa with $N_f = 1.27 \times 10^8$ cycles under ultrasonic frequency fatigue loading at $R = 0.1$. (a) SEM image of the fracture surface. (b) Close-ups of crack initiation and early growth region (red rectangle) in (a), in which the rectangle in (b) denotes the location where the micro-sample is extracted. (c) SEM image in the FIB milling process. (d) SEM image of the micro-sample. (e) Band contrast (BC) map of the extracted micro-sample superimposed by various twin boundaries and low-angle grain boundaries (LAGBs, 2°–10°). (f)–(h) Phase map, IPF-X, and KAM map of the extracted sample, respectively. (For interpretation of the references to color in this figure legend, the reader is referred to the web version of this article.)

from the ultrasonic specimen.

After that, the quasi in-situ specimen was conducted for 1.01×10^5 cycles at $\sigma_{max} = 750$ MPa by SERVO-SEM, and then observed by SEM and EBSD for tracking the microstructure evolution. The results are shown in Fig. 5h–k. Finally, this quasi in-situ specimen was conducted at a higher maximum stress $\sigma_{max} = 900$ MPa and is failed at 6.56×10^3 cycles. Fig. 5b and 5c show the SEM image of part of the quasi in-situ specimen after failure. The associated SEM and EBSD results are shown in Fig. 5l–o.

A comparison of the results in Fig. 5h–k with the ones in Fig. 5d–g indicates that there is no change for the grain size, occurrence of twinning, and crystallographic orientation after 1.01×10^5 loading cycles at the maximum stress $\sigma_{max} = 750$ MPa. Two possible reasons is responsible for this. One is that the crack initiation or microstructure evolution that can induce the crack initiation does not occur or cannot be discriminated by EBSD observation for the AM Ti-6Al-4V alloy at the tested stress level. The other is that the crack initiation or microstructure evolution that can induce the crack initiation only occurs in the local region due to the low fatigue loading. Therefore, this local change of crack initiation or microstructure evolution could not be observed in a random region of ~100 μm × 100 μm. For this reason, the quasi in-situ specimen in Fig. 3 was continuously tested at a higher maximum stress $\sigma_{max} = 900$ MPa for 6.56×10^3 cycles (i.e., failure), and the labelled region was observed by SEM and EBSD. The labelled region is 2.36 mm far from the fracture surface, which eliminates the influence of the crack or crack growth on the microstructure evolution. As shown in Fig. 3l and m, the microstructure changes in some local regions after the fatigue loadings at the higher maximum stress $\sigma_{max} = 900$ MPa. The slip, deformation twinning and nanograins appear. The significant increment of KAM values nearby the slip traces also indicates the heavy dislocation pile-ups at α grain boundaries (Fig. 5k and o). It is noted that the overall change of the color in IPFs before and after a certain number of fatigue loadings should be due to the small difference in the position of the sample on the holder when the EBSD observation is conducted.

4. Discussion

4.1. Nanograin formation mechanism

For a further understanding of the crystallographic characteristic of grains in the labelled region, Fig. 6 shows the slips and twinning systems of a total of 71 α grains for this region (i.e., the green rectangular region in Fig. 5l). Among these α grains in Fig. 6a, the slip occurs in 60 α grains, and the twinning occurs in 12 α grains. Four α grains (grains 10, 26, 38,

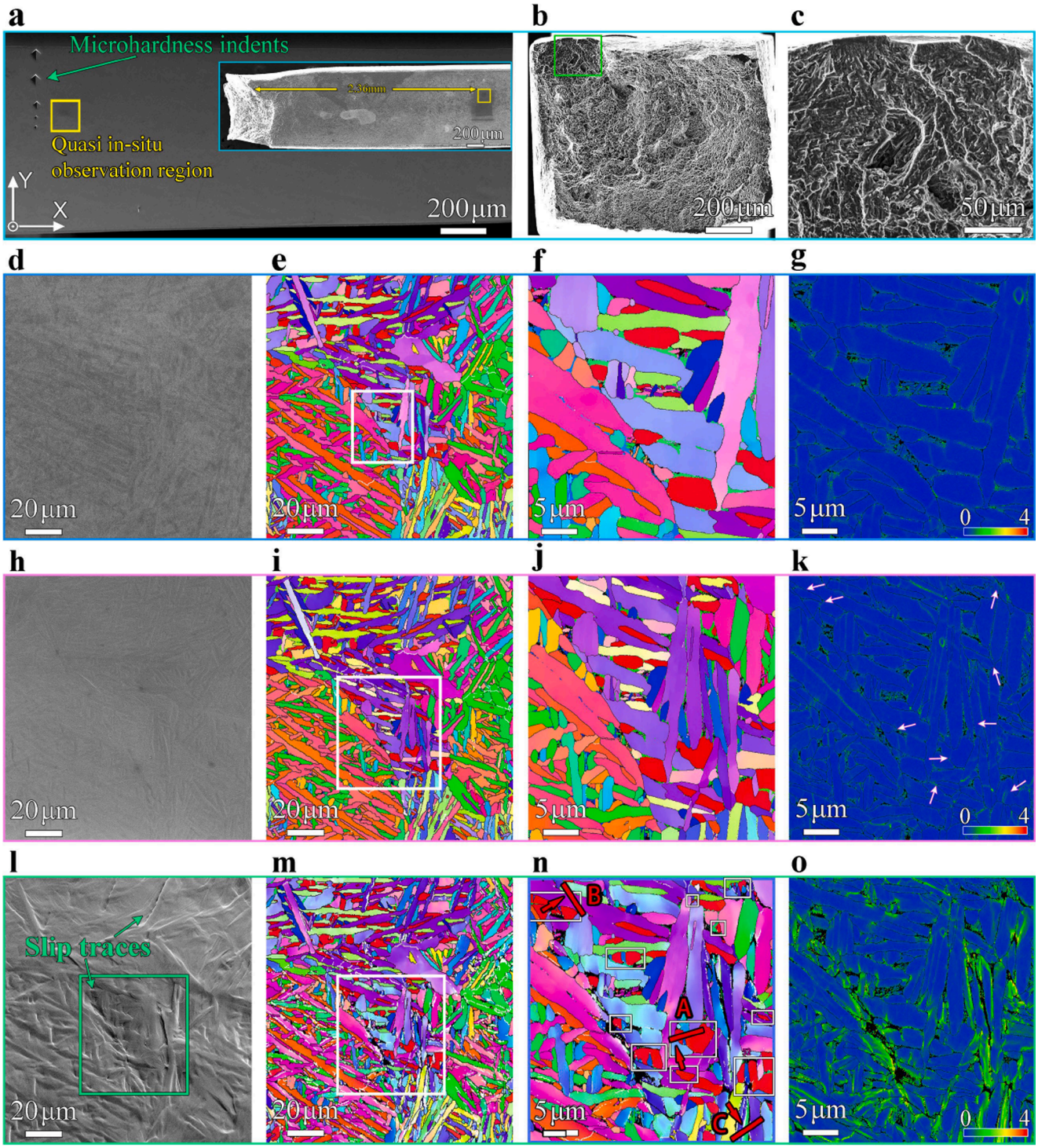

Fig. 5. Quasi in-situ observation of microstructure evolution during fatigue loadings. (a) SEM image of the quasi in-situ sample after 1.01×10^9 loading cycles at $\sigma_{max} = 750$ MPa under ultrasonic frequency fatigue test, in which the yellow rectangular region denotes the targeting region of observation. The figure in (a) is part of the SEM image of the extracted specimen after failure. (b) SEM image of the fracture surface of the quasi in-situ sample after failure. (c) Close-up of the green rectangular region in (b). (d) and (e) SEM image and IPF-X of the yellow rectangular region in (a), respectively. (f) and (g) Enlarged IPF-X and the associated KAM map of the white rectangle in (e), respectively. (h) and (i) SEM image and IPF-X of the yellow rectangular region in (a) after 1.01×10^5 loading cycles at $\sigma_{max} = 750$ MPa, respectively. (j) and (k) Enlarged IPF-X and the associated KAM map of the white rectangle in (i), respectively. (l) and (m) SEM image and IPF-X of the yellow rectangular region in (a) after 6.56×10^3 loading cycles at $\sigma_{max} = 900$ MPa, respectively. (n) and (o) Enlarged IPF-X and the associated KAM map of the white rectangle in (m), respectively. The short red lines in (n) indicate the extracted locations of the micro samples by FIB technique. The red arrows denote the observation direction in TKD and TEM. (For interpretation of the references to color in this figure legend, the reader is referred to the web version of this article.)

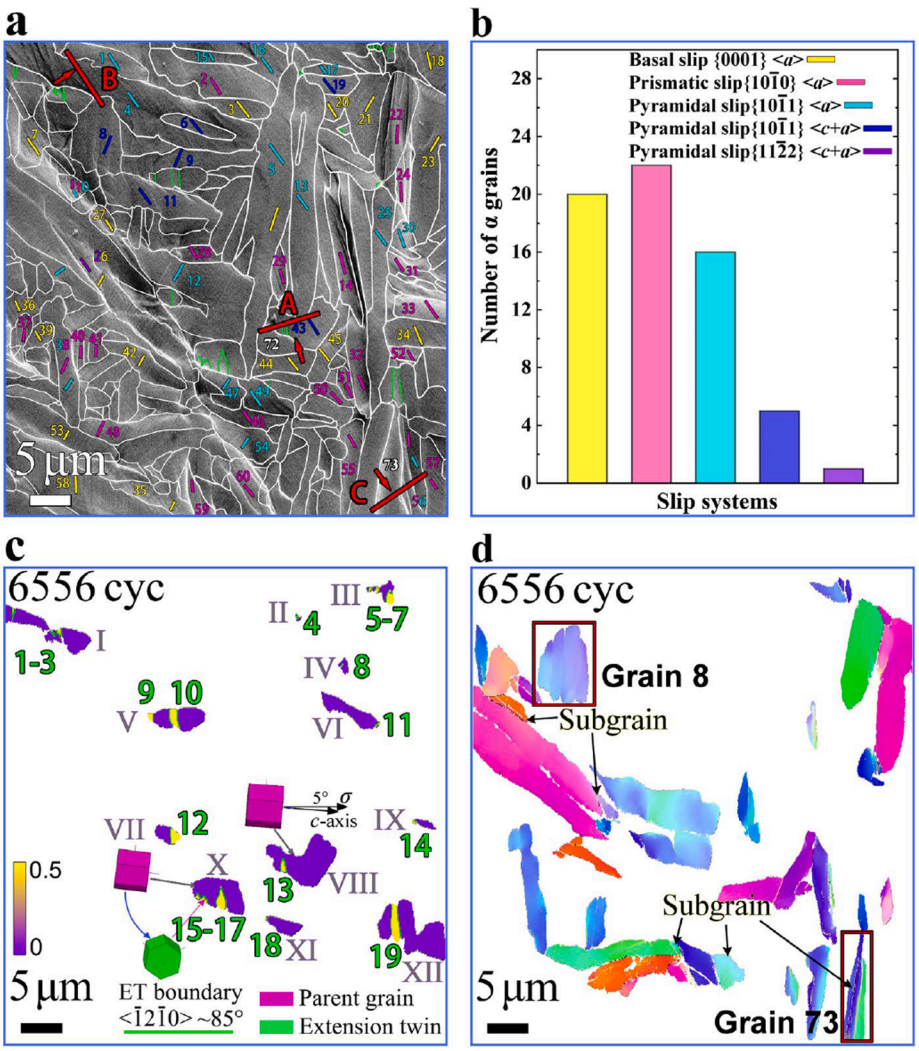

Fig. 6. Slips and twinning systems for the α grains in quasi in-situ region. (a) and (b) Slip traces and slip systems of the α grains in green rectangular region in Fig. 5l, in which the short red line in (a) shows the extracted locations of the micro samples by FIB technique and the red arrows denote the observation direction in TKD and TEM. (c) Schmid factors for the prismatic plane of "hard" α grains and twin variants in Fig. 5n. (d) IPF-X of refined grains with low-angle grain boundaries (LAGBs, 2°–10°) in Fig. 5n, in which the fine yellow lines represent the subgrain boundaries. (For interpretation of the references to color in this figure legend, the reader is referred to the web version of this article.)

and 56 in Fig. 6a) have cross slips, and one α grain (grain 43 in Fig. 6a) has pyramidal $\langle \boldsymbol{c}+\boldsymbol{a} \rangle$ slip and extension twinning.

The slip transmission depends on the surrounding grains, especially for the small grain size in polycrystalline Ti alloys [27]. The grains with the high Schmid factor of basal slip systems or prismatic slip systems are often called "soft grains" [28,29]. Here, the distinct slips are observed in most of the soft grains after the higher maximum stress $\sigma_{max} = 900$ MPa for 6.56×10^3 cycles, as shown in Figs. 5l and 6a. The predicted slip traces in Fig. 6a are at first calculated by MTEX software, and then the types of slip systems are confirmed by the Schmid factor and the slip

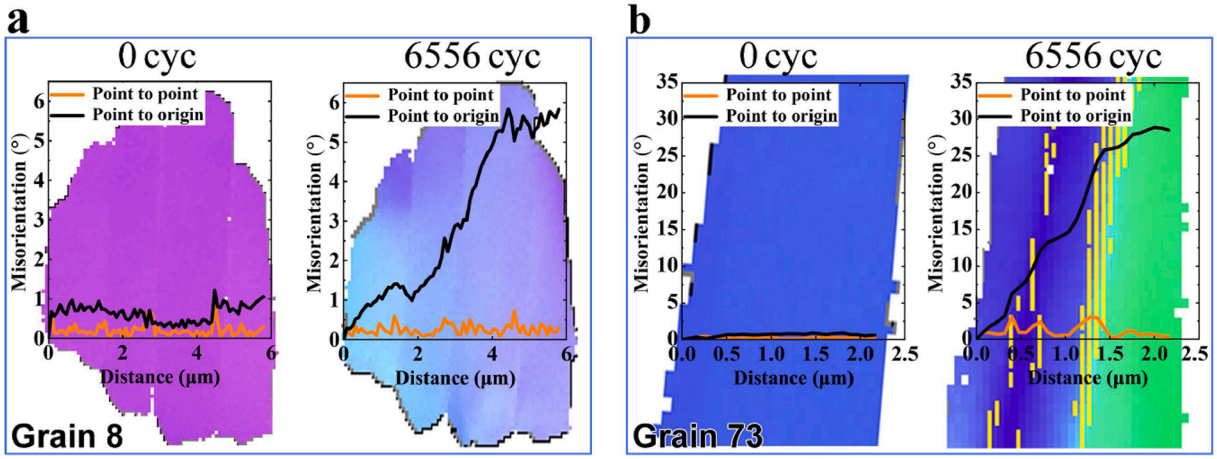

Fig. 7. In-grain misorientation profiles for soft grains. (a) In-grain misorientation profiles of grain 8 in Fig. 6d after 1.01×10^5 loading cycles at $\sigma_{max} = 750$ MPa (left figure) and after 6.56×10^3 loading cycles at $\sigma_{max} = 900$ MPa (right figure). (b) In-grain misorientation profiles of grain 73 in Fig. 6d after 1.01×10^5 loading cycles at $\sigma_{max} = 750$ MPa (left figure) and after 6.56×10^3 loading cycles at $\sigma_{max} = 900$ MPa (right figure).

traces observed on the SEM images. The experimental traces are considered to match the theoretical ones with the misorientation lower than 5°. Fig. 6b gives the statistics of slip systems in Fig. 6a, which indicates that the basal slips, prismatic slips, and pyramidal $\langle \boldsymbol{a} \rangle$ slips are the main slip types of α grains. The proportions are 28%, 31%, and 23%, respectively. The $\langle \boldsymbol{c}+\boldsymbol{a} \rangle$ pyramidal slips also occur in some α grains, and the proportion is 8%.

Moreover, a large number of subgrains and the increment of misorientations in α grains have been found in the labeled region after 6.56 × 10^3 loading cycles at σ_{max} = 900 MPa, as illustrated in Fig. 6d. Especially, Fig. 7a and b show the in-grain misorientation profiles for the two grains marked by red rectangles in Fig. 6d. The orange curve represents the misorientation relative to the previous point (i.e., MRPP), which can be used to determine the presence of LAGBs within the grain. The black curve represents the misorientation relative to the first point (i.e., MRFP), which indicates the accumulated change of misorientations, i.e., the degree of plastic deformation [30]. It is seen from Fig. 7a and b that there are many peaks in the MRPP curve with misorientation angles after 6.56 × 10^3 loading cycles at σ_{max} = 900 MPa, suggesting the presence of LAGBs. Actually, the lattice dislocations rearrange in soft grains by slipping or forming dense dislocation walls (DDWs) and dislocation tangles (DTs) inside the grains to minimize the total energy state. This creates dislocation cells that are confined by low angle boundaries (<1∘, shown as the MRPP curves in Fig. 7a). With continuous deformation, further rearrangement and annihilation of the dislocations occurs, creating subgrain boundaries with a higher misorientation angle compared to the DDWs, and the transformation of DDWs and DTs into sub-boundaries leads to the separation of individual cells or subgrains by absorbing more and more dislocation to minimize the total system energy [31]. The process of subgrain deformation is indicated in Fig. 7b where the MRFP is significantly increased for these two grains and the monotonic angle is over 25° around ⟨0001⟩ axle for these two subgrains in grain 73. However, the changing trend of the MRFP curve in Fig. 7b shows that the internal misorientation of the separated subgrains is very small, indicating that the subgrain boundaries absorb dislocations and the pile-up dislocations in the vicinity of the grain boundaries rearrange to form refined grains with LAGBs to further reduce the stress concentration when the dislocations exceed the capacity of absorption [31–33].

On the other hand, "hard grains'' have their *c*-axis nearly parallel to the applied stress (Fig. 6c), and the prismatic slip is difficult to occur due to very low Schmid factors [28,29,34]. It is found that twinning deformation has occurred in all hard α grains in Fig. 5n (i.e., the α grains in red color in IPF-X in the white rectangular region in Fig. 5n). The angle between the *c*-axis of α grains and the loading direction is in the range of 5°–10°. The KAM values where the arrows point in Fig. 5k indicate that the plastic deformation tends to accumulate between hard grain and soft grain boundaries during fatigue loadings and trigger the twinning when the plastic strain accumulation reaches a certain level, which provides the powerful evidence that the local high stress during fatigue loadings drives the twin nucleation in α grains [25,28,35]. Moreover, all the 12 deformation twins are {10$\bar{1}$2} ⟨$\bar{1}$011⟩ extension twins (as shown in Fig. 6c), which means that {10$\bar{1}$2} ⟨$\bar{1}$011⟩ extension twinning tends to activate under the macroscopic tension stress along the *c*-axis. The twin variants have a larger prismatic Schmid factor compared with the parent grains (Fig. 6c), and they are more suitable for the following plastic deformation through crystal slip. The similar slip-stimulated {10$\bar{1}$2} ⟨$\bar{1}$011⟩ extension twinning was also reported under dwell fatigue loadings [34,36]. In VHCF regime, the nanograins resulting from deformation twinning was also found in traditional forged TC17 alloy [18]. The twinning system and dislocation interaction could also cause the formation of dislocation cells, walls or microbands, and then the low angle and polygonal subgrains, and finally the nanograins in α grains of Ti alloys [32].

The refined α grains are measured and they are also compared with the original α grain. The results are shown in Fig. 8, in which the grain size is represented by the circle equivalent diameter of grains. It is seen from Fig. 8a that the original α grains are all larger than 1 μm and they are mostly distributed from 1 to 11 μm. While the sizes of twin variants are all smaller than 2 μm, and the sizes of the formed subgrains are distributed from 0 to 6 μm, as shown in Fig. 8a and b.

The TKD results of the three extracted samples in Fig. 5n or Fig. 6a are illustrated in Fig. 9. The sample A includes grain 43 with twinning occurrence in Fig. 6a and the grain 72 is on its left. The twin variant in grain 43 has grown from the specimen surface to α-β boundary at the bottom, as shown in Fig. 9a–d. The results in Fig. 9e–h indicate that the deformation of the grain 4 in Fig. 6a with surface slip trace is relatively greater. The sample C includes grain 73 with subgrain formation in Fig. 6a. However, no clear subgrain boundaries are observed inside the specimen for grain 73 from the TKD results. The misorientation between the left and right changes gradually. This will be discussed in detail in the subsequent TEM observations.

Fig. 10a shows the bright field TEM image of sample A in Fig. 9a, in which the twin variant near the crack surface can be observed. Fig. 10b is the bright field image close to the [2$\bar{1}\bar{1}$0] zone axis with a diffraction vector of $\boldsymbol{g}$ = [01$\bar{1}$2]for the twinning region (i.e., grain 43 in Fig. 6a) in Fig. 10a, in which the selected area electron diffraction (SAED) patterns of the twin variant and the associated parent grain at the orange circle is inserted at the bottom right corner in Fig. 10b. The twin variant was identified as {10$\bar{1}$2} twin by the SAED pattern along the zone axis of [2$\bar{1}\bar{1}$0] which shows a measured orientation relationship of $(0\bar{1}12)_m$//$(01\bar{1}2)_t$. HRTEM observations were conducted to further characterize the TB structure in Fig. 10b, as shown in Fig. 10d. It is seen that the {10$\bar{1}$2} TBs present a stepped-and-serrated structure consisting of one P_mB_t (i.e., $(0\bar{1}10)_m$//$(0002)_t$)-CTB (i.e., $(0\bar{1}12)_m$//$(01\bar{1}2)_t$) step in

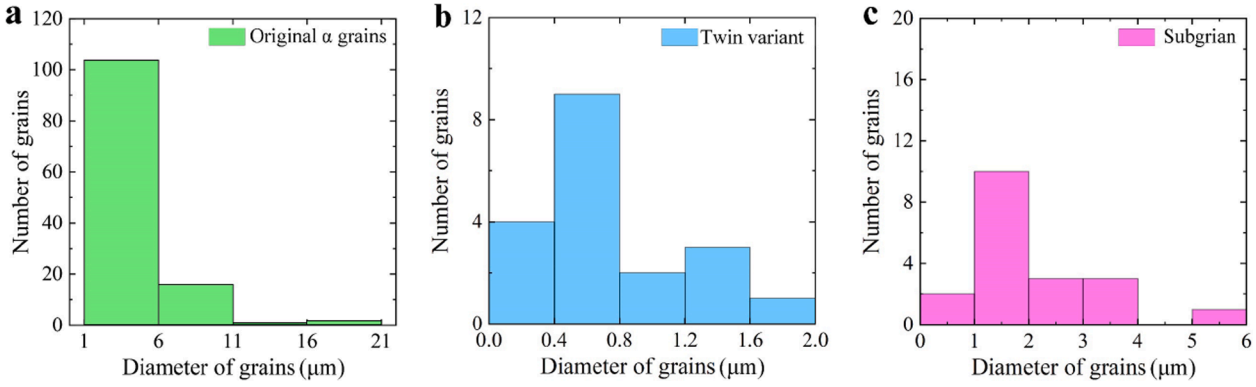

Fig. 8. Grain size distribution of original α grains and refined α grains in quasi in-situ observed region. (a) Original α grains in Fig. 6a. (b) Twin variants in Fig. 6c. (c) Subgrains in Fig. 6d.

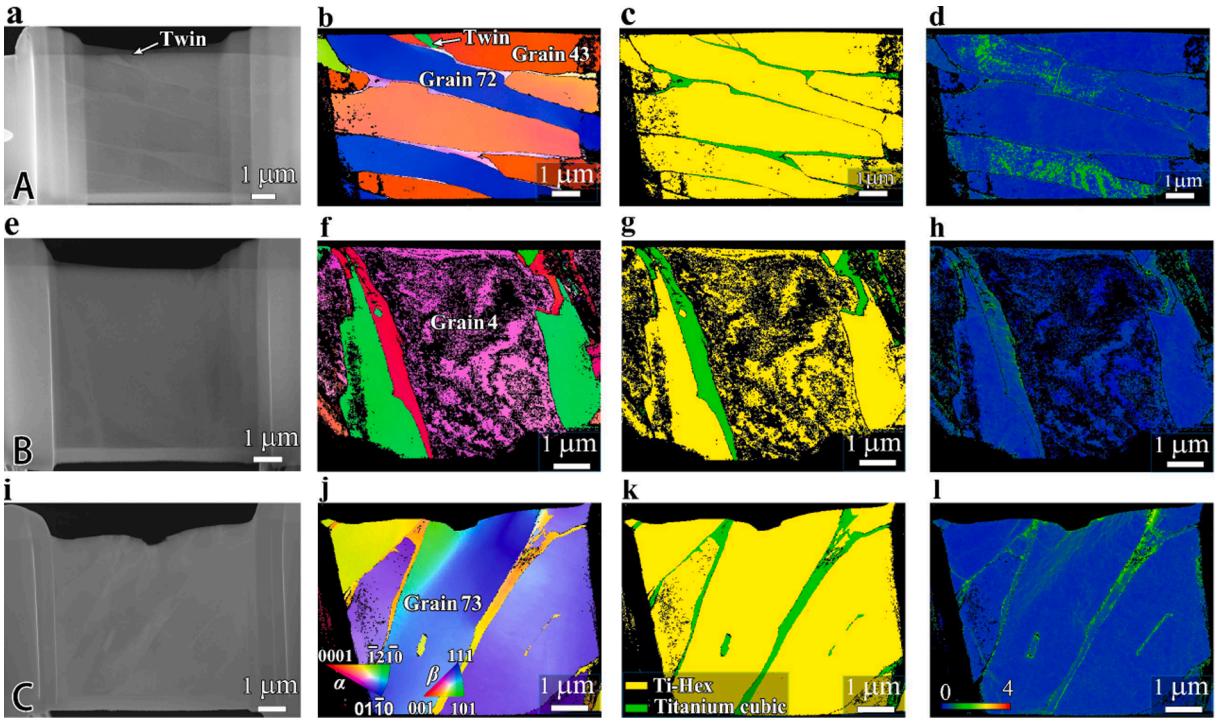

Fig. 9. SEM and TKD observations of the three extracted samples in Fig. 5n or Fig. 6a. (a)–(d) SEM image, IPF-X, phase map, and KAM map of sample A in Fig. 6a, respectively. (e)–(h) SEM image, IPF-X, phase map, and KAM map of sample B in Fig. 6a, respectively. (i)–(l) SEM image, IPF-X, phase map, and KAM map of sample C in Fig. 6a, respectively.

atomic scale, and one P_mB_t-CTB-B_mP_t (i.e., $(0002)_m//(0\bar{1}10)_t$) serration between the parent grain and twin variant. The P_mB_t-CTB step and P_mB_t-CTB-B_mP_t serrations lead to the deviation of the actual twin boundary from the theoretical $\{10\bar{1}2\}$ invariant plane (i.e., CTB). It is reported that the serrated twin boundary is related to the localized strain field and pileup of twinning dislocation [37,38]. The serrated interface structure leads to relatively small strain [39], and the coherent P_mB_t and B_mP_t boundaries are energetically stable [37,40–42].

Moreover, the extensive stacking faults (SFs) were observed inside the twin variant in Fig. 10b, and their direction was parallel to the direction of {0002} plane of the twin variant. The SFs in Fig. 10b are always connected to the incoherent TBs. Fig. 10f and g are the inverse fast Fourier transformation showing that the (0002) lattice planes of the red and green rectangular region in Fig. 10d, respectively, which indicates the basal dislocations for the parent grain shown by the red arrows in Fig. 10f and the SFs for the twin variant shown by the green arrows in Fig. 10g. The dislocations emission from P_mB_t and B_mP_t boundaries induces the occurrence of such basal SFs during fatigue loadings, similar to that observed for magnesium alloys under uniaxial compressive test [43].

Fig. 10c and e show that grain 72 contains a large density of dislocations at the two-beam dark field image with the condition of $\boldsymbol{g} = [01\bar{1}1]$ unlike the matrix of grain 43. The $\langle 11\bar{2}0\rangle$ of grain 72 is close to the loading direction from the IPF-X in Fig. 5n, indicating that it is a "soft grain". The results in Fig. 10c and e indicate that the dislocation tends to pile-up in "soft grain" during fatigue loadings.

It is known that $\langle \boldsymbol{c}+\boldsymbol{a}\rangle$ dislocation is difficult to occur in HCP structure since a larger critical resolve shear stress is required than that for twinning or $\langle \boldsymbol{a}\rangle$ dislocation slip [44–46]. However, the results in Fig. 6 indicate that many pyramidal slips appear in low cycle fatigue regime. Here, the TEM observation is used to further validate the pyramidal slip for the present AM Ti-6Al-4V alloy. Fig. 11a shows the bright field TEM image of sample B in Fig. 9e, and Fig. 11b is the SAED pattern inside grain 4 shown in Fig. 11a. Fig. 11c, e, and g are the two-beam condition dark field images for the same region when the foil is tilted close to $[2\bar{1}\bar{1}0]$ zone axis with $\boldsymbol{g}=[01\bar{1}1]$, $\boldsymbol{g}=[01\bar{1}\bar{1}]$, and $\boldsymbol{g}=[0002]$, and Fig. 11d, f, and h are the associated bright field images, respectively. According to $\boldsymbol{g}\cdot\boldsymbol{b}=0$ invisible criterion [47–49], when $\boldsymbol{g}=[01\bar{1}1]$or $\boldsymbol{g}=[01\bar{1}\bar{1}]$is applied, both $\langle \boldsymbol{a}\rangle$ and $\langle \boldsymbol{c}+\boldsymbol{a}\rangle$ type dislocations can be observed. This corresponds to the situation in Fig. 11c–f. Moreover, most prominent dislocations in Fig. 11c–f are long and straight, which are aligned in the same direction and parallel to the (0002) plane denoted by blue dash lines. This means that these dislocations lie on the basal plane. Besides, the $\langle \boldsymbol{a}\rangle$ type dislocations are invisible when the same region is characterized under two-beam condition with the diffraction vector $\boldsymbol{g}=[0002]$. This is the case in Fig. 11g and h. Therefore, the $\langle \boldsymbol{a}\rangle$ type dislocations lying on basal plane were activated. By combining the $[2\bar{1}\bar{1}0]$ zone axis with the orientation of grain 4 in Fig. 5n, the slip trace on the sample surface is caused by the $\langle \boldsymbol{a}\rangle$ type dislocation slipping in the pyramidal $\{10\bar{1}1\}$ plane.

Fig. 12 shows the TEM results for the sample C in Fig. 9i. It is observed that the dislocations accumulate heavily within grain 73 in Fig. 12a, and there are equal inclination fringes within grain 73 in Fig. 12b. These equal inclination fringes should be attributed to the gradual variation in orientation within the grain considering the thinness (~100 nm) and flatness of the sample, which is consistent with the EBSD results in Fig. 9j that the internal orientation difference changes progressively from left to right in grain 73. Further, a significant entanglement and accumulation of dislocations and dislocation walls are observed in grain 73.

The misorientation inside grain 73 is also analyzed by employing TEM observation in this study. Firstly, the region enclosed by the red circle 2 in Fig. 12c was aligned to the center of the screen. At this point, the beam was parallel to the zone axis $[2\bar{1}\bar{1}3]$, and the camera constant was $L = 300$ nm. The diffraction pattern is shown in Fig. 12e. Subsequently, the position of the red circle 1 in Fig. 12c was moved to the center of the screen, and L was adjusted to 100 nm. Finally, the misorientation between positions 1 and 2 was calculated using the formula $\tan 2\theta = R/L$ (where θ is scattering semi-angle, R is the distance on screen between diffraction spots), resulting in a value of 7.5°. Similarly,

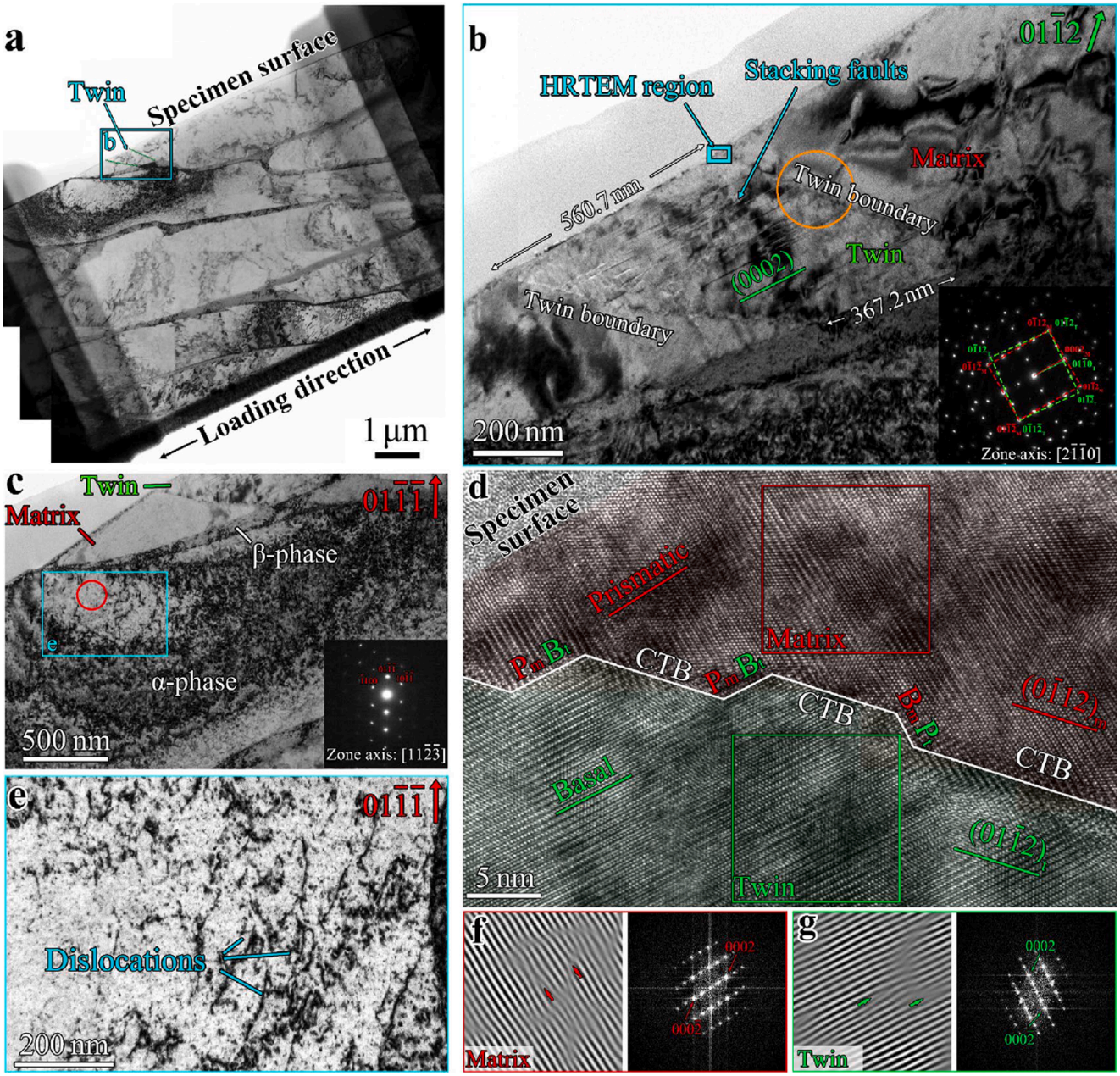

Fig. 10. TEM characterization for sample A in Fig. 9a. (a) Bright field image. (b) Bright field two-beam images of the dislocations with $\boldsymbol{g} = [01\bar{1}2]$ at twinning region, where the SAED pattern at TBs is inserted at the right bottom. (c) Two-beam condition dark field image for grain 43 in Fig. 6a when the foil is tilted close to $[11\bar{2}3]$ using $\boldsymbol{g}$=$[01\bar{1}\bar{1}]$, where the SAED pattern is inserted at the right bottom. (e) Enlargement of the blue rectangular region in (c). (d) HRTEM image of "HRTEM region" in (b). (f) Inverse fast Fourier transform image of the red rectangular region in (d) showing the (0002) lattice planes. (g) Inverse fast Fourier transform image of the green rectangular region in (d) showing the (0002) lattice planes. (For interpretation of the references to color in this figure legend, the reader is referred to the web version of this article.)

the misorientation between position 3 and position 2 in Fig. 12c was determined to be 8.0°. For detailed principles and procedures, please refer to the references [47,50]. The results in Fig. 12 indicate that the action of fatigue loadings could lead to the motion and accumulation of dislocations inside α grains, and then the formation of dislocation cells or walls, and finally the subgrains or very small grains with bigger orientation differences.

4.2. Relationship between nanograins and crack initiation

The quasi in-situ observed results show that the nanograins form during low cycle fatigue loadings in AM Ti-6Al-4V alloy and the twinning and slip are both contributors to the nanograin formation. The formation of nanograins in Ti alloys has also been shown in HCF and VHCF regimes [18,51–54]. The fracture surface of the quasi in-situ specimen after 6.56×10^3 loading cycles at $\sigma_{max} = 900$ MPa is further observed, as shown in Fig. 5b and 5c. It is seen that there is a small crack initiation and growth region on the fracture surface. The FGA feature is not found in the crack initiation and early growth region as that observed in VHCF regime (Fig. 5c). This implies that the nanograins formed during fatigue loadings tend to enhance the resistance of crack initiation in low cycle fatigue regime. This is in agreement with the results that the fatigue crack tends to initiate at α-β interface, larger α-phase, etc. under relatively higher stress levels [12,13,55]. It also

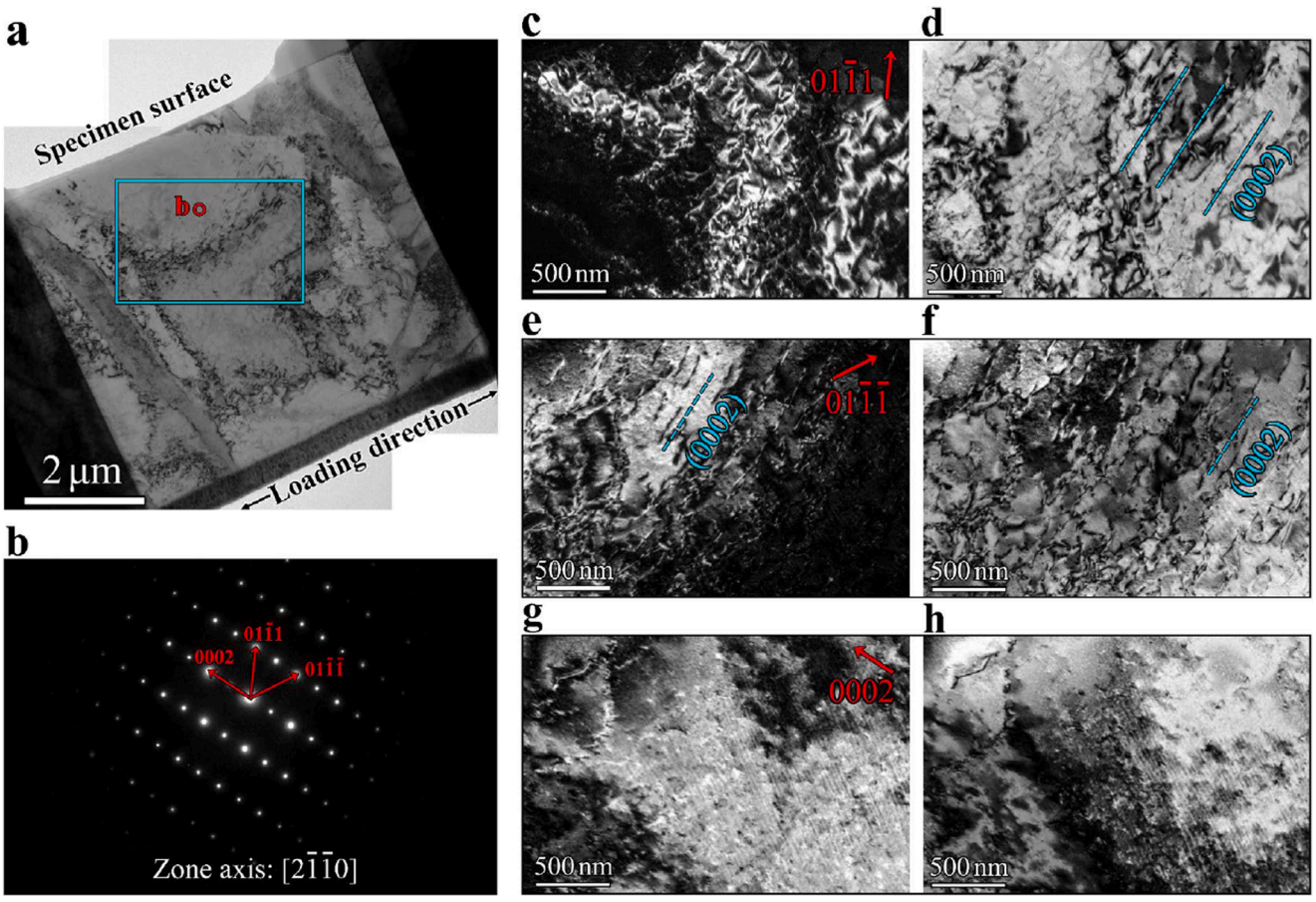

Fig. 11. TEM characterization for sample B in Fig. 9e. (a) Bright field image, in which the blue rectangular region is for TEM observation under two-beam diffraction conditions. (b) SAED pattern for the region in red circle in (a). (c) and (d) Two-beam condition dark and bright field images when the foil is tilted close to [$2\bar{1}\bar{1}$0] with $\boldsymbol{g}$=[$01\bar{1}1$], respectively. (e) and (f) Two-beam condition dark and bright field image when the foil is tilted close to [$2\bar{1}\bar{1}$0] with $\boldsymbol{g}$=[$01\bar{1}\bar{1}$], respectively. (g) and (h) Two-beam condition dark and bright field image when the foil is tilted close to [$2\bar{1}\bar{1}$0] with $\boldsymbol{g}$=[0002], respectively. (c)–(h) are all for the same blue rectangular region in (a). The diffraction vector is at the right top of each dark field image. (For interpretation of the references to color in this figure legend, the reader is referred to the web version of this article.)

accords with the results that the titanium with coarse grains presents poor fatigue performance than that of the titanium with ultrafine grains in HCF regime and this difference disappears in VHCF regime [56].

Previous studies have shown that the nanograins formed during fatigue loadings play a vital role in the crack initiation and early growth of titanium alloys and high strength steels in VHCF regime [10,18,57–59]. The cyclic strain localization has also been observed at very low stress amplitude over a large number of loading cycles ($>10^{10}$) [23]. The deformation twins and nanograins observed in the crack initiation and early growth region of the present AM Ti-6Al-4V alloy in Fig. 4 further implies that the twinning or slip due to the local high stress can induce the formation of local subgrains and then the nanograins in preferentially oriented α grains after a number of loading cycles although the stress amplitude is relatively low in VHCF regime [18]. The formation of nanograins increases the microstructural inhomogeneity and stress concentration in local regions and promotes the VHCF crack initiation and growth [18,56,60].

5. Conclusions

In summary, the quasi in-situ EBSD observation was successfully achieved and used for the direct observation of the process of nanograin formation during fatigue loadings in AM Ti-6Al-4V alloy in this paper. The main conclusions of this study are as follows:

(1) The deformation twinning and slip-induced subgrains are both contributors to the nanograin formation during fatigue loadings. The deformation twinning and nanograins can form in α grains in the crack initiation and early growth region at positive stress ratios in VHCF regime.

(2) The dislocations prefer to occur in soft α grains during fatigue loadings, and the basal slips, prismatic slips, and pyramidal ⟨$\boldsymbol{a}$⟩ slips are the prior slip types. While in hard α grains (e.g., the angle between the *c*-axis and the loading direction is <10°), it prefers to activate {$10\bar{1}2$} ⟨$\bar{1}011$⟩ extension twinning for coordinating the deformation. The twin boundary with stepped-like section of P_mB_t-CTB step and P_mB_t-CTB-B_mP_t serration is observed during fatigue loadings, which is responsible for the deviation of the actual twin boundary from the theoretical {$10\bar{1}2$} twin boundary.

(3) The nanograins formed during the fatigue loading increase the microstructural inhomogeneity in local regions and promote the crack initiation and growth in VHCF regime, which results in the final failure under the low applied axial stress.

CRediT authorship contribution statement

Weiqian Chi: Methodology, Investigation, Writing – review & editing. **Wenjing Wang:** Investigation, Writing – review & editing, Funding acquisition. **Lei Wu:** Writing – review & editing. **Guihua Duan:** Writing – review & editing. **Chengqi Sun:** Conceptualization,

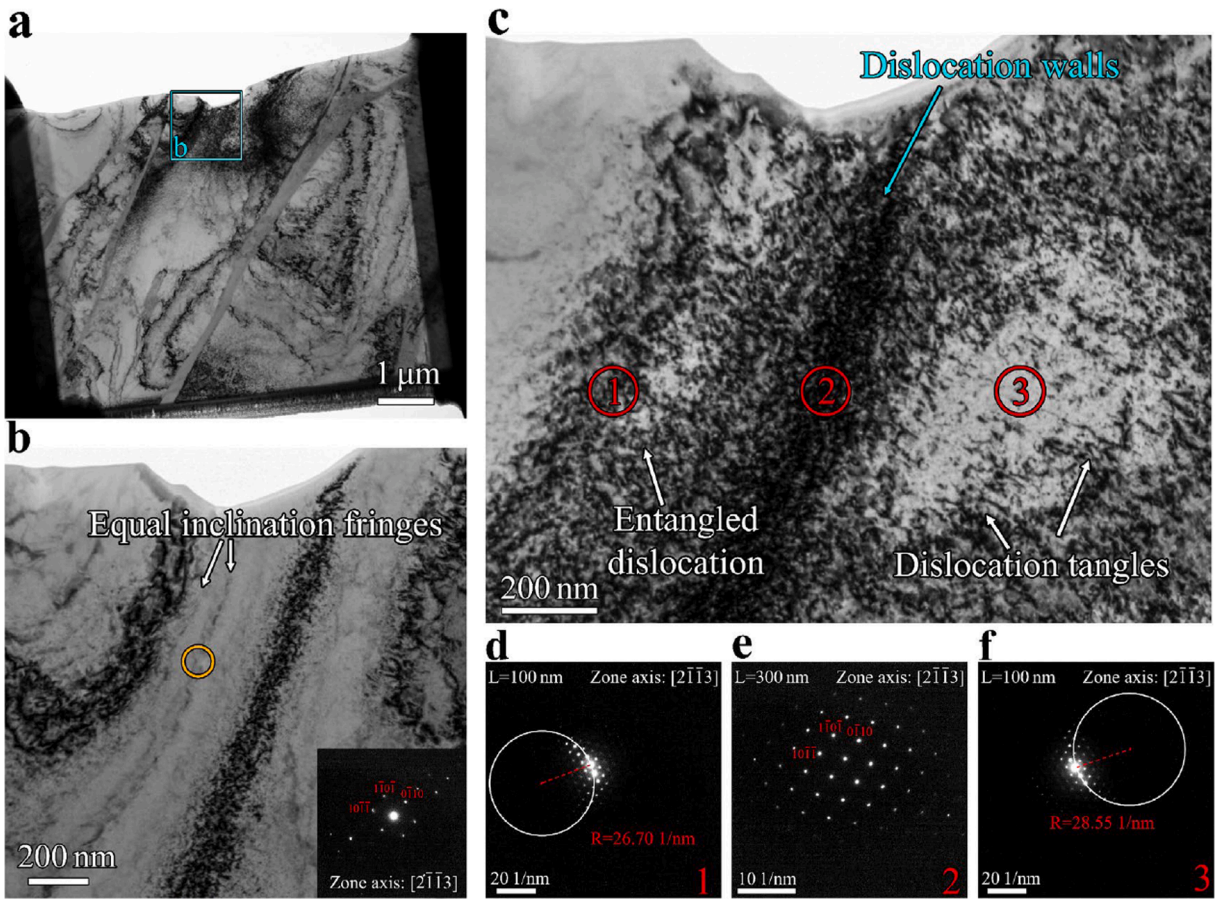

Fig. 12. TEM characterization for sample C in Fig. 9i. (a) Bright field image. (b) Enlargement of the blue rectangular region in (a), where the SAED by the orange circles in (b) is at the bottom right corner. (c) The bright-field image in (b) corresponds to a position near the sample surface when the zone axils//[2$\bar{1}\bar{1}$3]. (d-f): The SAED of the red circles 1, 2, and 3 in (c), with camera constants $L = 100$ nm, 300 nm, and 100 nm, respectively. (For interpretation of the references to color in this figure legend, the reader is referred to the web version of this article.)

Methodology, Investigation, Writing – review & editing, Funding acquisition, Supervision.

Declaration of Competing Interest

The authors declare that they have no known competing financial interests or personal relationships that could have appeared to influence the work reported in this paper.

Data availability

Data will be made available on request.

Acknowledgements

The authors acknowledge the support of the National Natural Science Foundation of China Basic Science Center for "Multiscale Problems in Nonlinear Mechanics" (11988102), the National Natural Science Foundation of China (91860112, 52075032) and Science and Technology Research and Development Program of China State Railway Group Co., Ltd. (K2022J003). The authors are also deeply grateful to Dr. Min Zhang for providing valuable help in TEM analysis.

References

[1] Liu G, Zhang X, Chen X, He Y, Cheng L, Huo M, et al. Additive manufacturing of structural materials. Mater Sci Eng R Reports 2021;145:100596.
[2] Tan C, Weng F, Sui S, Chew Y, Bi G. Progress and perspectives in laser additive manufacturing of key aeroengine materials. Int J Mach Tools Manuf 2021;170:103804.
[3] Avateffazeli M, Haghshenas M. Ultrasonic fatigue of laser beam powder bed fused metals: a state-of-the-art review. Eng Fail Anal 2022;134:106015.
[4] Molaei R, Fatemi A, Sanaei N, Pegues J, Shamsaei N, Shao S, et al. Fatigue of additive manufactured Ti-6Al-4V, Part II: The relationship between microstructure, material cyclic properties, and component performance. Int J Fatigue 2020;132:105363.
[5] Sun C, Chi W, Wang W, Duan Y. Characteristic and mechanism of crack initiation and early growth of an additively manufactured Ti-6Al-4V in very high cycle fatigue regime. Int J Mech Sci 2021;205:106591.
[6] Li P, Warner DH, Pegues JW, Roach MD, Shamsaei N, Phan N. Investigation of the mechanisms by which hot isostatic pressing improves the fatigue performance of powder bed fused Ti-6Al-4V. Int J Fatigue 2019;120:342–52.
[7] Molaei R, Fatemi A, Phan N. Significance of hot isostatic pressing (HIP) on multiaxial deformation and fatigue behaviors of additive manufactured Ti-6Al-4V including build orientation and surface roughness effects. Int J Fatigue 2018;117:352–70.
[8] Shui X, Yamanaka K, Mori M, Nagata Y, Kurita K, Chiba A. Effects of post-processing on cyclic fatigue response of a titanium alloy additively manufactured by electron beam melting. Mater Sci Eng A 2017;680:239–48.
[9] Hong YS, Sun CQ. The nature and the mechanism of crack initiation and early growth for very-high-cycle fatigue of metallic materials - an overview. Theor Appl Fract Mech 2017;92:331–50.
[10] Chi W, Li G, Wang W, Sun C. Interior initiation and early growth of very high cycle fatigue crack in an additively manufactured Ti-alloy. Int J Fatigue 2022;160:106862.
[11] Bridier F, Villechaise P, Mendez J. Slip and fatigue crack formation processes in an α/β titanium alloy in relation to crystallographic texture on different scales. Acta Mater 2008;56:3951–62.
[12] Sasaoka S, Arakawa J, Akebono H, Sugeta A, Shirai Y, Nakayama E, et al. The effects of crystallographic orientation on fatigue crack initiation behavior in Ti-6Al-4V. Int J Fatigue 2018;117:371–83.

[13] Liu C, Thomas R, Sun T, Donoghue J, Zhang X, Burnett TL, et al. Multi-dimensional study of the effect of early slip activity on fatigue crack initiation in a near-a titanium alloy. Acta Mater 2022;223:117967.
[14] Pan X, Qian G, Hong Y. Nanograin formation in dimple ridges due to local severe-plastic-deformation during ductile fracture. Scr Mater 2021;194:113631.
[15] Oguma H. Formation mechanism of the distinctive granular fracture surface in subsurface fracture of Ti6Al4V alloy. Materialia 2022;21:101312.
[16] Gao G, Liu R, Fan Y, Qian G, Gui X, Misra RDK, et al. Mechanism of subsurface microstructural fatigue crack initiation during high and very-high cycle fatigue of advanced bainitic steels. J Mater Sci Technol 2022;108:142–57.
[17] Zhu ML, Jin L, Xuan FZ. Fatigue life and mechanistic modeling of interior micro-defect induced cracking in high cycle and very high cycle regimes. Acta Mater 2018;157:259–75.
[18] Sun C, Wu H, Chi W, Wang W, Zhang G-P. Nanograin formation and cracking mechanism in Ti alloys under very high cycle fatigue loading. Int J Fatigue 2023;167:107331.
[19] Heczko M, Mazánová V, Slone CE, Shih M, George EP, Ghazisaeidi M, et al. Role of deformation twinning in fatigue of CrCoNi medium-entropy alloy at room temperature. Scr Mater 2021;202:113985.
[20] Jamali A, Ma A, Llorca J. Influence of grain size and grain boundary misorientation on the fatigue crack initiation mechanisms of textured AZ31 Mg alloy. Scr Mater 2022;207:114304.
[21] Chi W, Wang W, Li Y, Xu W, Sun C. Defect induced cracking and modeling of fatigue strength for an additively manufactured Ti-6Al-4V alloy in very high cycle fatigue regime. Theor Appl Fract Mech 2022;119:103380.
[22] Sun C, Song Q. A method for predicting the effects of specimen geometry and loading condition on fatigue strength. Metals 2018;8(10):811.
[23] Weidner A, Amberger D, Pyczak F, Schönbauer B, Stanzl-Tschegg S, Mughrabi H. Fatigue damage in copper polycrystals subjected to ultrahigh-cycle fatigue below the PSB threshold. Int J Fatigue 2010;32:872–8.
[24] Zhang K, Zheng J-H, Huang Y, Pruncu C, Jiang J. Evolution of twinning and shear bands in magnesium alloys during rolling at room and cryogenic temperature. Mater Des 2020;193:108793.
[25] Choi S-W, Won JW, Lee S, Hong JK, Choi YS. Deformation twinning activity and twin structure development of pure titanium at cryogenic temperature. Mater Sci Eng A 2018;738:75–80.
[26] Sun J, Peng W, Sun C. Mechanism of artificial surface defect induced cracking for very high cycle fatigue of Ti alloys. Eng Fract Mech 2022;272:108721.
[27] Kacher J, Eftink BP, Cui B, Robertson IM. Dislocation interactions with grain boundaries. Curr Opin Solid State Mater Sci 2014;18:227–43.
[28] Wang L, Yang Y, Eisenlohr P, Bieler TR, Crimp MA, Mason DE. Twin nucleation by slip transfer across grain boundaries in commercial purity titanium. Metall Mater Trans A 2009;41:421.
[29] Dunne FPE, Walker A, Rugg D. A systematic study of hcp crystal orientation and morphology effects in polycrystal deformation and fatigue. Proc R Soc A Math Phys Eng Sci 2007;463:1467–89.
[30] Zhao PC, Chen B, Zheng ZG, Guan B, Zhang XC, Tu ST. Microstructure and texture evolution in a post-dynamic recrystallized titanium during annealing, monotonic and cyclic loading. Metall Mater Trans A 2021;52:394–412.
[31] Tao NR, Wang ZB, Tong WP, Sui ML, Lu J, Lu K. An investigation of surface nanocrystallization mechanism in Fe induced by surface mechanical attrition treatment. Acta Mater 2002;50:4603–16.
[32] Zhu KY, Vassel A, Brisset F, Lu K, Lu J. Nanostructure formation mechanism of α-titanium using SMAT. Acta Mater 2004;52:4101–10.
[33] Tan JC, Tan MJ. Dynamic continuous recrystallization characteristics in two stage deformation of Mg–3Al–1Zn alloy sheet. Mater Sci Eng A 2003;339:124–32.
[34] Lavogiez C, Hémery S, Villechaise P. Analysis of deformation mechanisms operating under fatigue and dwell-fatigue loadings in an α/β titanium alloy. Int J Fatigue 2020;131:105341.
[35] Jia Y, Jiang S, Tan J, Lu Z, Jiang J, Wang X. The evolution of local stress during deformation twinning in a Mg-Gd-Y-Zn alloy. Acta Mater 2022;222:117452.
[36] Lavogiez C, Hémery S, Villechaise P. Concurrent operation of ⟨c + a⟩ slip and twinning under cyclic loading of Ti-6Al-4V. Scr Mater 2018;157:30–3.
[37] Wei B, Ni S, Liu Y, Song M. Structural characterization of the 112¯2 twin boundary and the corresponding stress accommodation mechanisms in pure titanium. J Mater Sci Technol 2021;72:114–21.
[38] Gong M, Hirth JP, Liu Y, Shen Y, Wang J. Interface structures and twinning mechanisms of twins in hexagonal metals. Mater Res Lett 2017;5:449–64.
[39] Zhang M, Qiu J, Shi Z, Tan Z. Serrated and stepped-like twin boundary of nano-sized extension twin in a deformed magnesium alloy. Mater Lett 2019;236:604–6.
[40] Liao X, Wang J, Nie J, Jiang Y, Wu P. Deformation twinning in hexagonal materials. MRS Bull 2016;41:314–9.
[41] Zhang J, Xi G, Wan X, Fang C. The dislocation-twin interaction and evolution of twin boundary in AZ31 Mg alloy. Acta Mater 2017;133:208–16.
[42] He Y, Li B, Wang C, Mao SX. Direct observation of dual-step twinning nucleation in hexagonal close-packed crystals. Nat Commun 2020;11:2483.
[43] Sun Q, Zhang X, Shu Y, Tan L, Liu Q. Two types of basal stacking faults within 101¯2 twin in deformed magnesium alloy. Mater Lett 2016;185:355–8.
[44] Yoo MH. Slip, twinning, and fracture in hexagonal close-packed metals. Metall Trans A 1981;12:409–18.
[45] Britton TB, Dunne FPE, Wilkinson AJ. On the mechanistic basis of deformation at the microscale in hexagonal close-packed metals. Proc R Soc A Math Phys Eng Sci 2015;471:20140881.
[46] Yoo MH, Lee JK. Deformation twinning in h.c.p. metals and alloys. Philos Mag A 1991;63:987–1000.
[47] Williams DB, Barry C. Carter. Transmission electron microscopy: a textbook for materials science; 2009.
[48] Xie KY, Reddy KM, Ma L, Caffee A, Chen M, Hemker KJ. Experimental observations of the mechanisms associated with the high hardening and low strain to failure of magnesium. Materialia 2019;8:100504.
[49] Zhu Y, Hou D, Chen K, Wang Z. Loading direction dependence of asymmetric response of <c+a> pyramidal slip in rolled AZ31 magnesium alloy. J Magnes Alloy 2022.
[50] Wu J, Howe JM, Zhang WZ. An in situ transmission electron microscopy study of interface growth during martensitic transformation in an Fe–Ni–Mn alloy. Acta Mater 2011;59:3297–303.
[51] Li G, Ke L, Ren X, Sun C. High cycle and very high cycle fatigue of TC17 titanium alloy: stress ratio effect and fatigue strength modeling. Int J Fatigue 2023;166:107299.
[52] Li G, Sun C. High-temperature failure mechanism and defect sensitivity of TC17 titanium alloy in high cycle fatigue. J Mater Sci Technol 2022;122:128–40.
[53] Wu H, Chi W, Xu W, Wang W, Sun C. Effects of specimen geometry and surface defect on high and very high cycle fatigue of TC17 alloy. Eng Fract Mech 2022;276:108940.
[54] Pan X, Xu S, Qian G, Nikitin A, Shanyavskiy A, Palin-Luc T, et al. The mechanism of internal fatigue-crack initiation and early growth in a titanium alloy with lamellar and equiaxed microstructure. Mater Sci Eng A 2020;798:140110.
[55] Sun C, Li Y, Huang R, Wang L, Liu J, Zhou L, et al. Crack initiation mechanism and fatigue life of titanium alloy Ti–6Al–2Sn–2Zr–3Mo-X: Effects of stress ratio and loading frequency. Mater Sci Eng A 2020;798:140265.
[56] Sajadifar SV, Wegener T, Yapici GG, Niendorf T. Effect of grain size on the very high cycle fatigue behavior and notch sensitivity of titanium. Theor Appl Fract Mech 2019;104:102362.
[57] Grad P, Reuscher B, Brodyanski A, Kopnarski M, Kerscher E. Mechanism of fatigue crack initiation and propagation in the very high cycle fatigue regime of high-strength steels. Scr Mater 2012;67:838–41.
[58] Sun C, Song Q, Zhou L, Liu J, Wang Y, Wu X, et al. The formation of discontinuous gradient regimes during crack initiation in high strength steels under very high cycle fatigue. Int J Fatigue 2019;124:483–92.
[59] Wang C, Liu Y, Nikitin A, Wang Q, Zhou M. A general scenario of fish-eye crack initiation on the life of high-strength steels in the very high-cycle fatigue regime. Fatigue Fract Eng Mater Struct 2019;42:2183–94.
[60] Vinogradov A. Fatigue limit and crack growth in ultra-fine grain metals produced by severe plastic deformation. J Mater Sci 2007;42:1797–808.